

Article

In-Situ Study Methods Used in the Discovery of Sites of Modern Hydrothermal Ore Formation on the Mid-Atlantic Ridge

Sergei Sudarikov ^{1,2}, Vladimir Petrov ^{1,*}, Egor Narkevsky ³, Irina Dobretsova ³ and Irina Antipova ³¹ St. Petersburg Mining University, 2, 21st Line, St Petersburg 199106, Russia² VNIOkeangeologia, Angliyskiy Av., 1, St. Petersburg 190121, Russia³ Polar Marine Geosurvey Expedition, Lomonosov, Pobedy 24, St. Petersburg 198412, Russia

* Correspondence: vladimir@spmi-petrov.ru

Abstract: This paper presents in situ methods used in the search for areas of modern hydrothermal activity, as well as the results of their long-term use during cruises within the Russian exploration area of the Mid-Atlantic Ridge (MAR). In this study, the following methods were used: CTD-sounding, methane sounding, teleprofiling and measurements with Eh, pS, pNa, pH and EF sensors. During profiling by towed complexes (RIFT, MAK-1M), various geophysical and geochemical anomalies near high-temperature, low-temperature and inactive fields were detected. Geophysical anomalies are more distinct when profiling near the bottom, and geochemical anomalies are located at a distance from the bottom (~150–200 m). Direct signs of high-temperature discharging (black smoker's smoke, hydrothermal buildings) and indirect signs of low-temperature discharging (lithified carbonate sediments and accumulations of endemic hydrothermal fauna) were detected during teleprofiling. We have described 6 types of complex geophysical anomalies determined by CTD-sounding that allow the detection of plumes at different stages of formation and from different sources. The use of a methane sensor during sounding makes it more likely to identify a low-temperature discharge. Methane has a highly variable nature of distribution—over distances from the first hundreds of meters to tens of kilometers and a seabed height of ~50–500 m. The use of these methods together makes it more possible to detect low- and high-temperature hydrothermal discharges within mid-oceanic ridges (MOR).

Keywords: Mid-Atlantic Ridge; bottom waters; profiling; CTD-sounding; hydrothermal plume; hydrothermal systems; geochemistry; seafloor massive sulfides



Citation: Sudarikov, S.; Petrov, V.; Narkevsky, E.; Dobretsova, I.; Antipova, I. In-Situ Study Methods Used in the Discovery of Sites of Modern Hydrothermal Ore Formation on the Mid-Atlantic Ridge. *Minerals* **2022**, *12*, 1219. <https://doi.org/10.3390/min12101219>

Academic Editors: Kunfeng Qiu and Callum Hetherington

Received: 31 August 2022

Accepted: 22 September 2022

Published: 27 September 2022

Publisher's Note: MDPI stays neutral with regard to jurisdictional claims in published maps and institutional affiliations.



Copyright: © 2022 by the authors. Licensee MDPI, Basel, Switzerland. This article is an open access article distributed under the terms and conditions of the Creative Commons Attribution (CC BY) license (<https://creativecommons.org/licenses/by/4.0/>).

1. Introduction

Deep-sea hydrothermal vents are specific dynamic systems characterized by sharp chemical and physical gradients [1]. Since the discovery of the first hydrothermal source [2], interest in deep-sea hydrothermal systems has not decreased over the past few decades [3]. Numerous objective reasons can explain the attention paid to hydrothermal systems.

First, it is of economic interest since deposits of polymetallic sulfides are confined to the areas of modern deep-sea hydrothermal activity [4,5]. The development of such deposits will significantly expand the resource base [6].

Second, hydrothermal fields (HF) remain an “oasis of life,” supplying not only trace elements necessary for the existence of numerous endemic organisms [1,7], but also several potentially dangerous compounds [8].

Third, a comprehensive study of hydrothermal systems makes it possible to reconstruct the paleo-conditions of the deep-sea parts of the ancient oceans and can help determine the structure and chemical composition of waters in the past [9].

The main search sign is a hydrothermal plume [1] formed when a hot acidic hydrothermal solution is discharged into the oceanic water column [10]. The actual boundaries of plumes are difficult to determine due to lateral dispersion [11]. The incoming hydrothermal

solution is enriched with metals (Mn, Fe, Cu, Zn and others), gases (CH₄, H₂, H₂S, and others) and various organic compounds [12–16], creating geophysical and geochemical anomalies in the water. Metal concentrations (and, respectively, anomalies) in hydrothermal solutions differ, since the process of their leaching is not constant because the rock is the realization of a spatially distributed random function of the initial concentration field, conditions and mechanisms of crystallization [17].

Due to the large depth (up to 4000 m and deeper), small size and strong variability of the geochemical and geophysical anomalies in time and space [18,19], it is most advantageous to use in-situ methods for HF's detection-profiling and sounding. Search methods have different sensitivities and limited use [1]. The application of a restricted number of methods can lead to erroneous results and increase the expenditure of time and resources. Comprehensive studies using several methods have made it possible to determine the existence and location of hydrothermal sources [20].

Here, we present the results of the application of these methods during a comprehensive study in the Russian exploration area (REA) of MAR for a long period. Based on the conducted studies, we identified the characteristic features of various anomalies, indicating a different type of hydrothermal discharge and the composition of the incoming solution.

Currently, within REA (12°48'36''–20°54'36'' N), 10 HF's have been discovered: Irinovskoye [21,22], Krasnov [23,24], Peterburgskoye [25], Zenit-Victoria [26], Yubileinoe [27], Puy des Folle [26], Surprise [27], Korolovoye, Molodezhnoye [28] and Holmistoe, and four hydrothermal clusters: Ashadze [26,29,30], Logachev [26,29,31,32], Pobeda [33,34] and Semenov [22,35] (Table 1). Average distances between fields on the MOR's vary in 12–220 km (from fast to ultra-slow spreading ridges). Based on the spreading rate within the REA (~25 mm/year), the distances between the fields should be 40–200 km (on average ~70 km) [36]. The distances between the HF's of the REA vary in a much larger interval (5.3–268.7 km), but on average, ~73.5 km. However, recent studies have shown that the distances between the fields within the fast- and medium-spreading MOR's are ~3.3–19 km [37], which is 3–6 times greater than expected (11–87 km) [36]. Thus, the distances between the fields within the slow-spreading ridges (MAR, in particular) may be much less than expected, which indicates a possible large number of undiscovered HF's within the REA. Including low-temperature ones, the number of which, according to some estimates, is at least ~25% [37].

Table 1. Hydrothermal fields and clusters within the REA and the distances between them (from south to north).

№	Name of the Object	N	W	Discovery Year	Distance between Fields, km
1	Ashadze cluster	12°58.40'	44°51.80'	2003	0
2	Korolovoye field	13°07.23'	44°53.84'	2020	16.77
3	Molodezhnoye field	13°09.34'	44°51.84'	2020	5.32
4	Irinovskoye field	13°19.97'	44°54.60'	2011	20.31
5	Semenov cluster	13°30.82'	44°57.78'	2007	20.91
6	Logachev cluster	14°42.50'	44°58.00'	1994	132.85
7	Krasnov field	16°38.40'	46°28.50'	2004	268.72
8	Pobeda cluster	17°09.00'	46°25.20'	2015	57.05
9	Holmistoe field	17°57.00'	46°29.30'	2014	89.25
10	Peterburgskoye field	19°52.00'	45°52.00'	2010	222.93
11	Zenit-Victoria field	20°07.75'	45°37.35'	2008	38.77
12	Yubileinoe field	20°09.00'	45°44.60'	2012	12.83
13	Puy des Folle field	20°30.50'	45°38.50'	2008	41.23
14	Surprise field	20°45.40'	45°38.60'	2012	27.61

2. Materials and Methods

2.1. Sounding of the Water Column

Sounding of the water column was carried out by the SBE 911plus sounding complex equipped with the SBE 17 SERAM memory unit as part of the CTD SBE 9plus submersible device and the onboard DU SBE 11plus unit. This complex is used to determine hydrostatic pressure, turbidity, electrical conductivity and temperature. The scanning frequency is 24 Hz. The parameters were determined from the surface to the bottom by the modernised tow-yo method—after sounding, the complex rose to the horizon of 1000 m, the vessel moved, and then the complex sank to the bottom again. The approach to the bottom was controlled by an altimeter, notifying when the distance from the bottom was reached in the range of 7–20 m. The positioning of the vessel during sounding was carried out using a thruster. The binding was carried out using the Sigma-1001 underwater navigation system.

Outboard operations were managed from the hydrological post. Descent and lifting operations were carried out from the winch through the hydraulic U-shaped portal. The descent of the probe was carried out on a cable 4.5 km long. The rate of descent was on average 1 m/s, and in the bottom (>1000 m) layer 0.5 m/s. The decrease in velocity in the bottom layer is due to the need to reduce the dynamic errors of the probe measurement channels and to improve the quality of measurement [28].

2.2. Sounding by a Methane Sensor

At the Logachev and Molodezhnoye and Korolovoye fields, standard CTD-sounding was accompanied by the measurement of CH₄ concentrations with a Franatech METS methane sensor. The detection range of the sensor is 1–500 nM. The maximum immersion depth is 4000 m [28].

2.3. Profiling by Towed Instrument Package

Measurement by sensors was carried out using the towed instrument package RIFT (until 2010) and the deep-sea geo-acoustic complex MAK-1M.

During the 7th, 25th and 26th cruises of the R/V “Professor Logachev” within the Logachev and Ashadze hydrothermal clusters, profiling with the RIFT complex was accompanied by measurements with Eh, pNa, pH and pS sensors [29,38,39].

The complex MAK-1M was used to perform a sonar survey of the bottom. Simultaneously, measurements of the potential of the natural electrical field (EF) on the profiles were conducted [34]. Since 2010, EF measurements have been carried out via two channels. Simultaneous use of two channels avoids loss of information in case of failure of electrodes. The distance between the upper and lower electrodes was 70 m. The height corridor from the bottom, in which the deep-sea vehicle was towed, averaged 80–90 m. The speed of the vessel was 1.2–1.5 knots, which provided acceptable conditions for profiling.

Transitions between profiles were carried out without lifting the device on board the vessel. The device was raised to such a level that the length of the cable was equal to the distance between the completed and the next profile, which avoids dangerous bends of the cable. Transitions between profiles were carried out not on adjacent profiles but through one or more profiles. This made it possible to conduct a safer turn for the cable.

The EF data were smoothed by the least squares method and straightened using the piecewise linear approximation method to exclude the influence of changes in the speed and depth of the device.

2.4. TV-Profiling

TV studies were conducted after the detection of EF anomalies to discover deep-sea polymetallic sulfides (DPS), to obtain terrain characteristics and to identify bottom organisms.

The TVSSperre television complex (SPERRE, Notodden, Norway) was used. The television complex consists of:

-High-resolution deep-sea camera HD (Sperre, Notodden, Norway). Main features: Full HD 1080i/60 resolution (1920 × 1080), 3.27 megapixels, sensitivity 0.03lx, digital zoom 12x, RS232 control.

-Deep-sea low-light camera (Sperre, Notodden, Norway). Main features: resolution 540 TVLs (795 × 596), sensitivity 0.051lx F1.2, digital zoom 12x, RS232 control.

-2 LED lamps Q-LED-III (ROS, San Diego, CA, USA). Main characteristics: light intensity 3500 lux, color temperature 5400 K, current consumption at 220 V at the input of 1.1 A, light flux width 80 × 80 degrees.

-Altimeter 1007D (Kongsberg Simrad Mesotech, Bergen, Norway). Main features: operating frequency 200 kHz, RS232 interface;

-Pressure sensor (Valeport MiniIPS, Totnes, UK). Main features: working depth-up to 6000 m, measurement accuracy ± 0.01% of the depth, resolution 0.0001 Bar (approximately 1 mm depth), RS232 interface.

The optimal distance from the bottom from the viewpoint of the safety of towing underwater vehicles and the quality of video materials is 2.5–3 m; simultaneously, the area of the observed section of the bottom is about 7–9 m². The towing speed of the device is 0.1–0.5 knots.

2.5. Hydroacoustic Underwater Positioning

The vessel was driven according to the profiles and sounding stations using a bow retractable rotary column and according to the HiPap-101 underwater navigation system (Kongsberg Maritime, Bergen, Norway). The Kongsberg CNode Mini transponder was integrated into the MAC-1M complex; on the rest of the devices, the transponders were attached with specially made mounts-holders to the frames of the devices.

3. Results and Discussion

3.1. Profiling by RIFT and MAK-1M

Profiling by towed vehicles is a standard method used to detect geophysical and geochemical anomalies. The origin of these anomalies in the bottom water is associated with processes occurring around the following: (1) ores surrounded by ion-conducting moisture-saturated rocks and (2) hydrothermal plumes.

The anomalous intervals of the EF values were taken to be those whose amplitude was at least 0.25 mV, which was three times higher than the standard deviation of the field values (background noise) outside the anomalous intervals.

3.1.1. Ashadze Hydrothermal Cluster

Eight and seventeen profiles were performed near the Ashadze-1 and Ashadze-2 HF's, respectively.

Several characteristic EF anomalies and weak Eh anomalies were noted on the profiles crossing the Ashadze-1 field (Figure 1). A decrease in Eh and a less distinct decrease in pH indicate the effect of high-temperature fluids on water [1]. The submeridional profile in Figure 1a is made 600 m east of the hydrothermal vent. The Eh anomaly was observed ~650 m to the NEE from the source, where, apparently, the current is directed. The EF anomaly is located ~1000 m to the NE from the source. Since the profiling was performed at 30–40 m from the bottom, it is likely that the device moved below the plume, which explains the weakness of the Eh anomaly.

The submeridional profiles in Figure 1b,c were obtained near the Ashadze-2 HF (12°59.5' N 44°54.4' W)—approximately 35–40 m to the east and west from the crater, respectively, at 110–150 m from the bottom.

The pS anomaly coinciding with Eh (Figure 1b) to the north of the source (~700 m) may indicate sulfide particles far from the source. To the SSW of the source (~460 m), the weaker Eh anomaly is not accompanied by a pS anomaly (Figure 1c). This is explained by the movement of the plume to the north of the source.

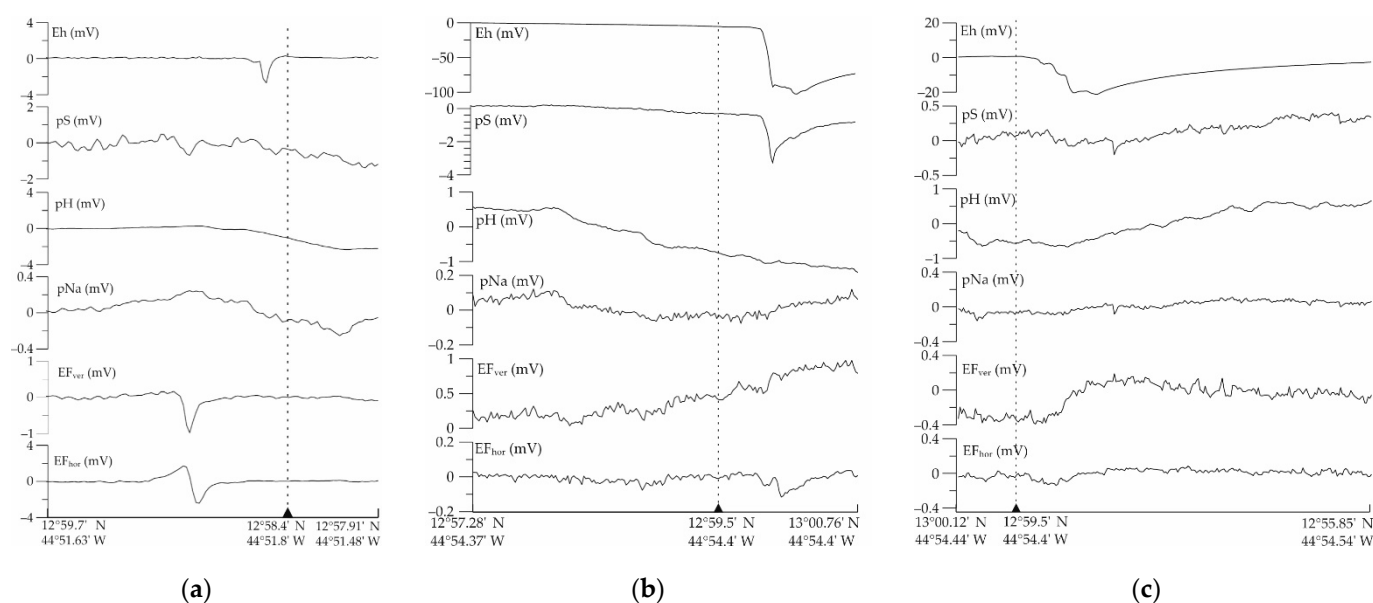


Figure 1. The results of profiling by EF (horizontal and vertical components), Eh, pH, pNa and pS sensors: (a) over the Ashadze-1 field at 30–40 m above the bottom; (b,c) over the Ashadze-2 field at 110–150 m above the bottom. The dotted line shows the position of the hydrothermal source.

The geochemical anomalies were accompanied by weak EF anomalies. The anomalies are faint and differ in shape from those detected near the bottom (Figure 1a). Most of the Eh anomalies are displaced relative to the EF anomalies by distances up to ~950–1000 m. The revealed Eh anomalies have the following features: a gradual decrease precedes a sharp decline. It is possible that the complex form of anomalies is associated with a blurred plume boundary.

3.1.2. Peterburgskoye, Semenov and Irinovskoye Hydrothermal Areas

The Peterburgskoye field was discovered in 2010 when the anomaly with an amplitude of ~1 mV was confirmed. Simultaneously, CTD-sounding did not reveal hydrothermal anomalies. Active high-temperature hydrothermal activity within the field ended about 63 thousand years ago [33]. Low-temperature discharge or magnetite and sulfide mineralization of rocks (because of hydrothermal discharge in the past) may cause EF anomalies in this case.

In 2011, about 15 anomalies within a range of 0.3–9 mV were detected in the area of the Semenov hydrothermal cluster, marking 5 HF's (Figure 2). EF anomalies reach large values both within the active and inactive hydrothermal sites.

To the south of the Semenov cluster, a new Irinovskoye field was discovered (Figure 2). Initially, the Irinovskoye field, despite well-marked EF anomalies, was deemed inactive. The age of its ores is ~7.8–69 thousand years, which indicates weak hydrothermal activity [33]. Nevertheless, two active sources were discovered in 2013 [21]. Apparently, hydrothermal activity within the Irinovskoye field has a sporadic character.

3.1.3. Pobeda Hydrothermal Cluster

Several EF anomalies with an intensity of at least 0.25 mV were detected in the area of 17°00'–17°10' N of the MAR (Figure 3).

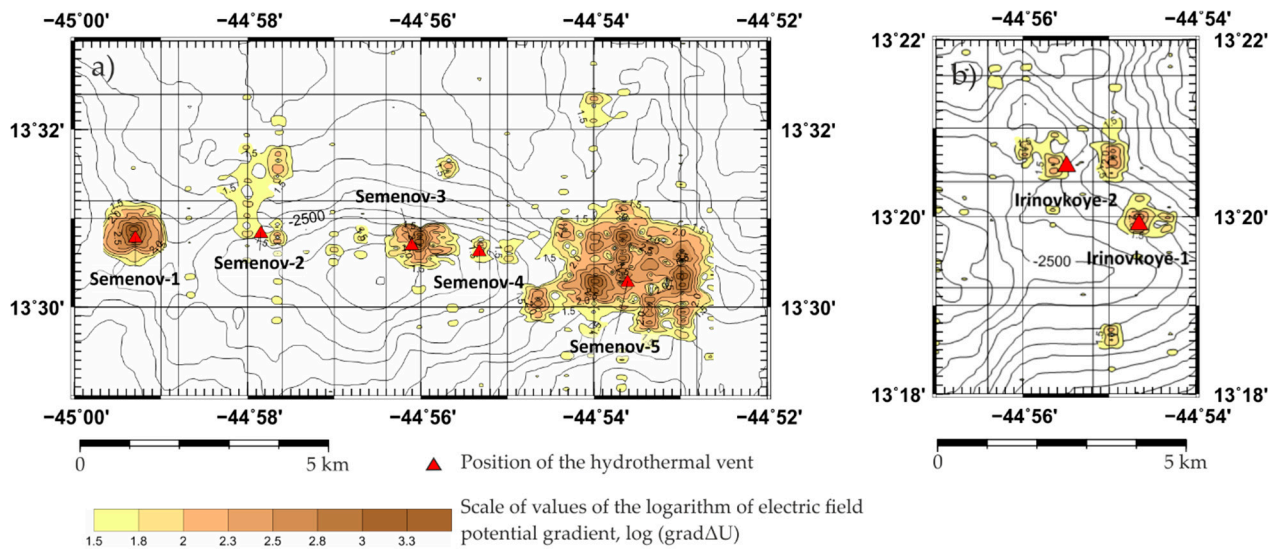


Figure 2. Schemes of isolines of the logarithm of the gradient ΔU : (a) the Semenov hydrothermal cluster; (b) the Irinovskoye HF.

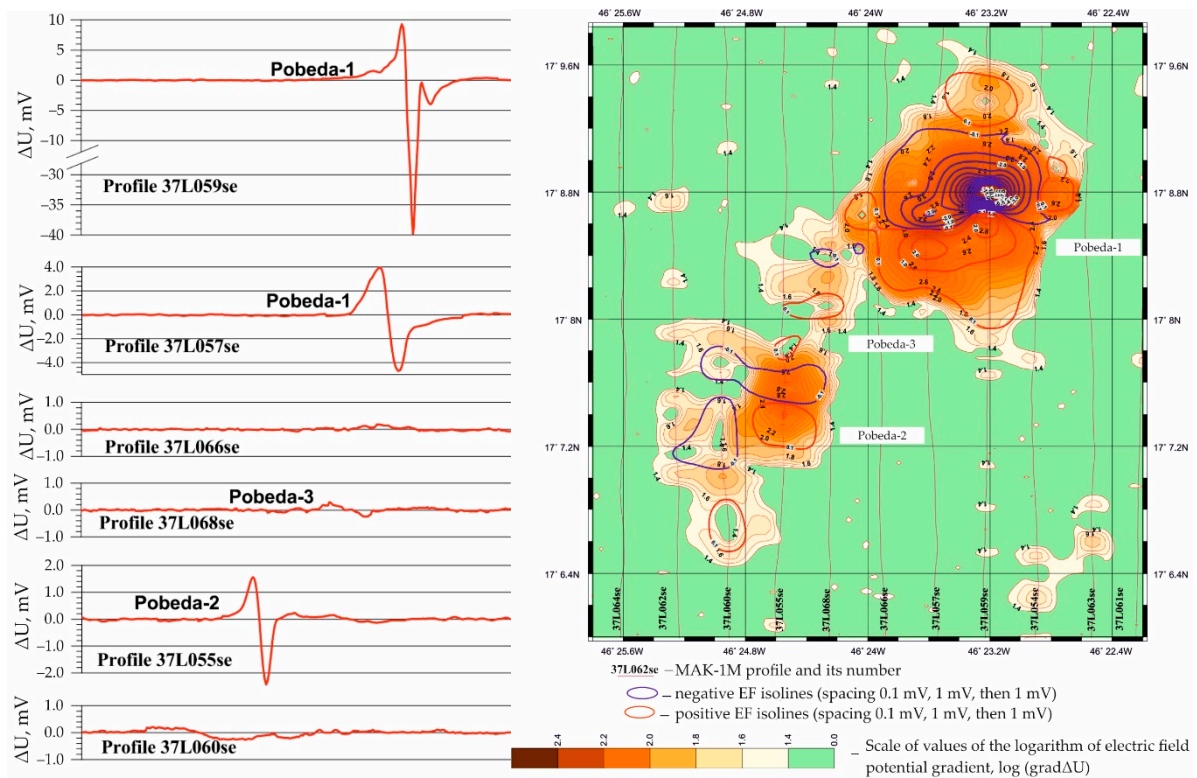


Figure 3. (Left) the EF anomalies near the Pobeda hydrothermal cluster; (right) combined scheme of isolines of the EF (ΔU) and the logarithm of the gradient ΔU , Pobeda hydrothermal cluster (modified after Gablina et al. [34]).

During the verification of two EF anomalies on profiles 37L57se and 37L59se, massive sulfide ores were sampled at several stations. Thus, Pobeda-1 HF was discovered.

The Pobeda-2 HF was discovered during dredging in the area of the EF anomaly established on profiles 37L055se and 37L060se (Figure 3), where massive sulfide ores, metalliferous sediments and hydrothermal crusts were raised. Additionally, along the 37L055se profile, the second profile was passed at a lower speed. The distance between the profiles was about 80 m. An EF anomaly of 12.3 mV intensity was detected. The intensity

of the anomaly has increased by more than 3 times, which underlines the importance of conducting work with the towing complex at a speed not exceeding 1.3 knots.

On profile 37L68se, metalliferous sediments and a fragment of breccia with abundant sulfide mineralization were raised. Perhaps this anomaly reflects the influence of the fields Pobeda-1 or Pobeda-2. It is also possible that there is another small ore object—the Pobeda-3 HF. All three objects constitute the Pobeda hydrothermal cluster.

Forty km SW of the Pobeda cluster, an EF anomaly was observed on profile 37L149se (16°49' N 46°37' W). TV observations and dredging revealed no obvious signs of hydrothermal activity. Nevertheless, a sufficiently high intensity of the anomaly (0.8 mV) provides grounds for detailed work. It is likely that inactive or low-temperature HF has been detected in this area, which is of interest for further research.

3.1.4. Molodezhnoye and Korolovoye HF's

Three well-localized EF anomalies and 8 weak anomalies were detected in the 13°05'–13°10' N of the MAR. Based on the results of profiling, a scheme of isolines of the logarithm of the gradient ΔU was constructed (Figure 4).

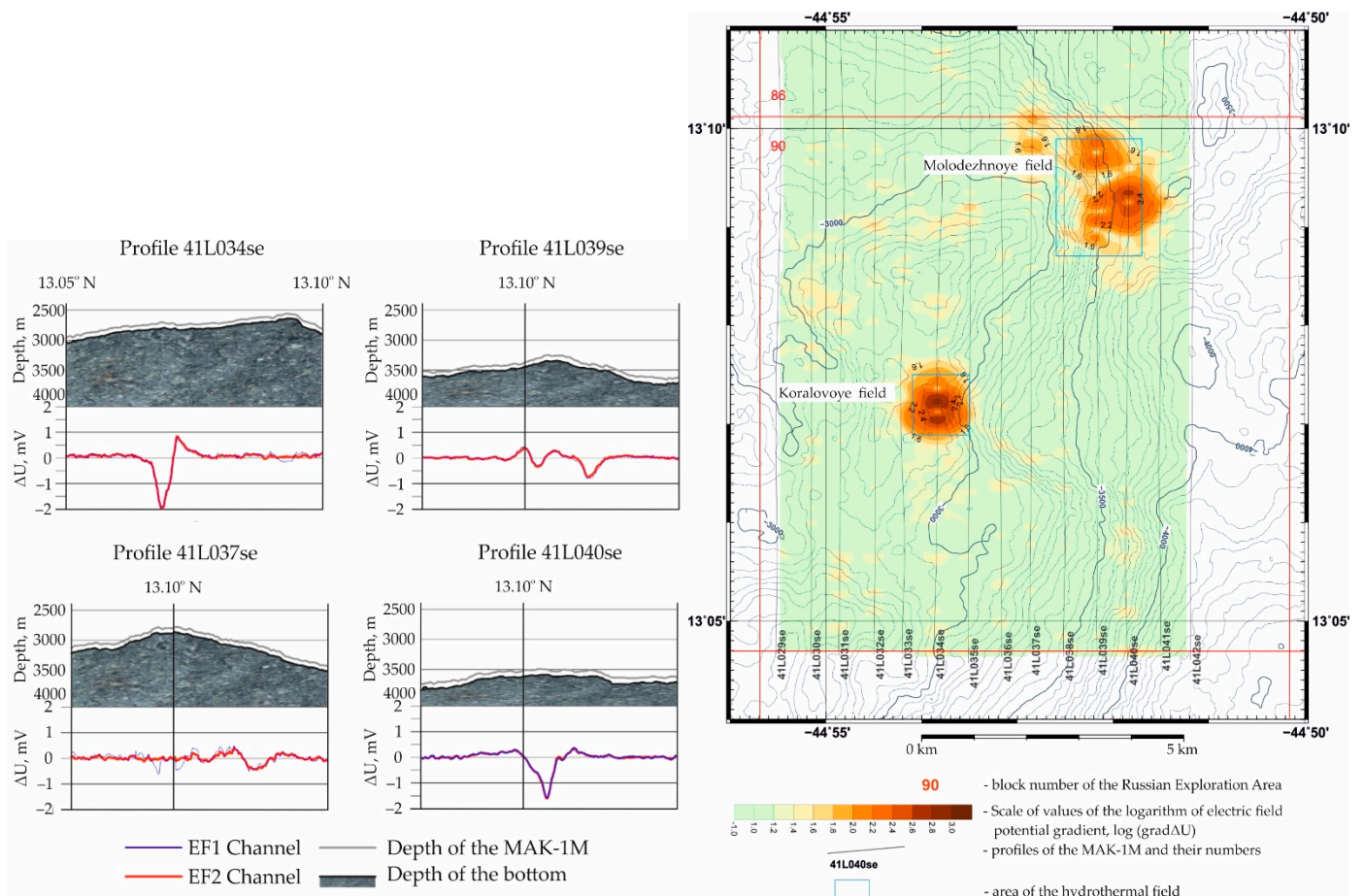


Figure 4. (Left) the EF anomalies on profiles; (right) scheme of the logarithm of the gradient ΔU . The Molodezhnoye and Korolovoye HF's.

The profiles 41L034se, 41L039se, 41L040se and 41L037se revealed intense anomalies of an obvious ore type, which allowed us to concentrate the points of geological testing here and identify two new Molodezhnoye and Korolovoye HF's. Active hydrothermal discharge forms a vast area (1 km or more) of EF anomalies. Such a large area may be due to the discharge of low-temperature diffusion sources around the main high-temperature source or the wide distribution of sulfide ores.

3.1.5. Logachev Hydrothermal Cluster

The EF, Eh and pS anomalies near Logachev HF were obtained at 15 m (E–W profiles) and 35 m (S–N profiles) from the bottom (Figure 5). The distance between the profiles was 250 and 500 m, respectively [38]. Fluctuations in the geophysical and geochemical parameters are synchronous and indicate a nearby local source. In the structure of the rising plume (Figure 6), spatial differentiation of the EF and Eh fields inside the plume is observed.

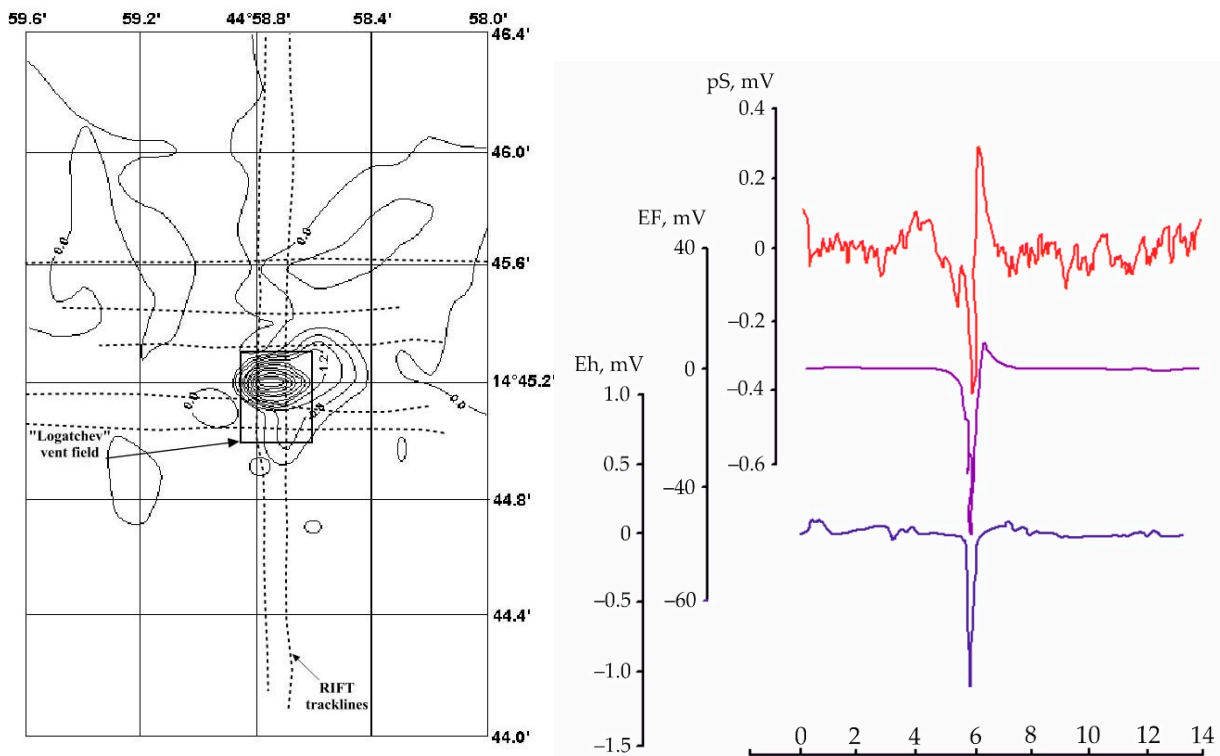


Figure 5. (Left) anomalies of the Eh at 15 m from the ocean floor [38]; (right) from bottom to top: anomalies of the Eh, EF and content of sulfide sulfur (pS) in the ascending (15 m above the bottom) hydrothermal plume of the Logachev field [40].

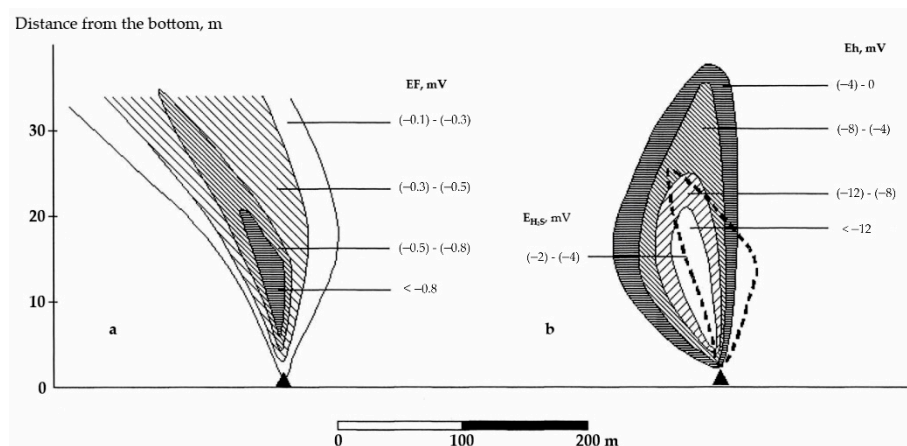


Figure 6. The structure of the geophysical ((a) EF) and geochemical ((b) Eh and E_{H2S}) anomalies above the active hydrothermal structure Irina-2 (Logachev field) [38].

The EF, Eh and EH₂S minima are found in the lower (~15 m) part of the plume. The low Eh associated with high sulfide concentrations is rather local. The rapid precipitation of most metals in the form of sulfide particles near the source [41] can explain the localization

of the Eh anomaly. The remaining dissolved metals (mainly Fe and Mn) were transported and precipitated as oxides and hydroxides [42]. Thus, the lower part of the plume is dominated by sulfides, while the upper part is dominated by Fe oxyhydroxides [42,43]. Since the near-bottom waters of the MAR are rich in oxygen (compared to the Pacific Ocean) [44], the increase in Eh can also be caused by the oxidation of H₂S remaining after the formation of sulfides.

Profiling at 200 m from the bottom also revealed distinct Eh and pS anomalies. The EF anomaly is weak at this distance and has an uncharacteristic shape (Figure 7). An atypical shape may be associated with the influence of a plume rather than an ore object.

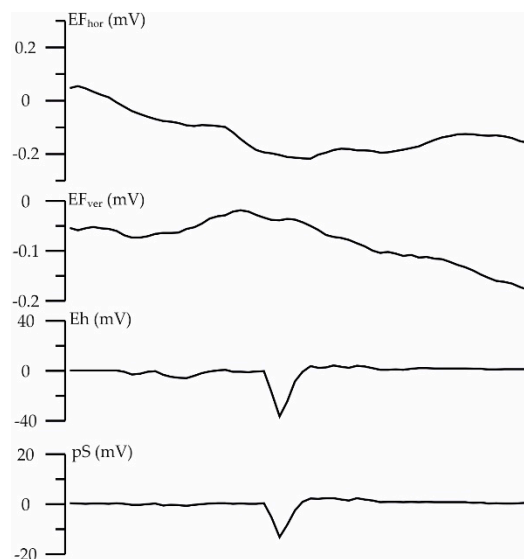


Figure 7. Anomalies EF (horizontal and vertical components), pS and Eh over the Logachev-1 field at 200 m from the bottom.

Based on all of the above, we conclude that EF anomalies are more frequently recorded near the bottom. Geochemical anomalies (Eh, pS) are often revealed at 150–200 m from the bottom.

Profiling should be divided into stages focused on identifying various anomalies. First, in the “high” interval, to identify the geochemical anomalies; second, in the “low” interval, to reveal EF anomalies. The EF anomalies in the “low” interval have an amplitude of several mV and a typical shape. Anomalies EF in the “high” interval not only have an amplitude several times smaller but also differ in shape. Perhaps they are associated not with the ores but with the influence of a hydrothermal plume. Sulfides recorded in the “high” interval can increase the EF at the interface between the plume and seawater.

The EF anomalies can indicate both high-temperature and low-temperature discharges. Several reasons may cause low-intensity EF anomalies: (1) scattered inclusions of ore minerals (sulfides, magnetite); (2) the peripheral part of intense anomalies of small size, located between the profiles; and (3) interference.

The Eh anomaly can be spatially close to the EF anomaly or located far enough away from it (~100–1000 m) (Figures 1, 6 and 7). This may be due to the detection of various stages of plume formation. Near the hydrothermal source, the plume does not spread and retains sharp boundaries, which contributes to the proximity of the Eh and EF anomalies.

For more accurate detection, it is best to reduce the distance between profiles. The anomalous section may be between the profiles—in this case, weak symmetrical anomalies on neighboring profiles may indicate this.

3.2. TV-Profilng

Television profiling makes it possible to detect and outline areas of modern hydrothermal activity. It is actively used in deep-sea and shallow-water studies of the ocean floor [1], 3D reconstruction, and modeling of the seabed [45].

The main signs of active hydrothermal discharge are hydrothermal buildings, their debris, and the “smoke” of smokers (Figure 8). TV observations do not detect areas of low-temperature activity since they do not form significant hydrothermal structures and do not produce the “smoke.”

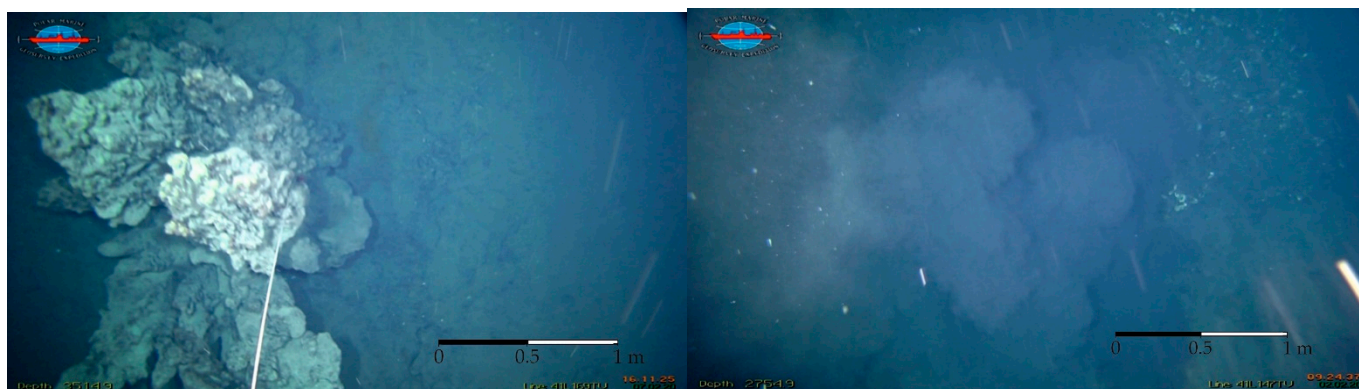


Figure 8. On the (left) a hydrothermal building in the area of the Molodezhnoye HF; on the (right) “smoke” from a black smoker in the area of the Koralovoye HF.

Nevertheless, teleprofiling can detect indirect signs of low-temperature discharge.

Near the Koralovoye HF, we noted a lithification in the flank of the fault below the slope and around a “hole” in the sediments (possibly, a low-temperature vent). Lithification is possibly caused by the transit of hydrothermal fluid through them (Figure 9). Fluid penetrates into the sediments and cools down because of mixing with seawater under subsurface conditions. In the process of fluid interaction with rocks, the cementation of sediments occurs due to the redeposition of carbonate material and the deposition of metal sulfides. Lithified sediments can be considered a sign of low-temperature discharging.

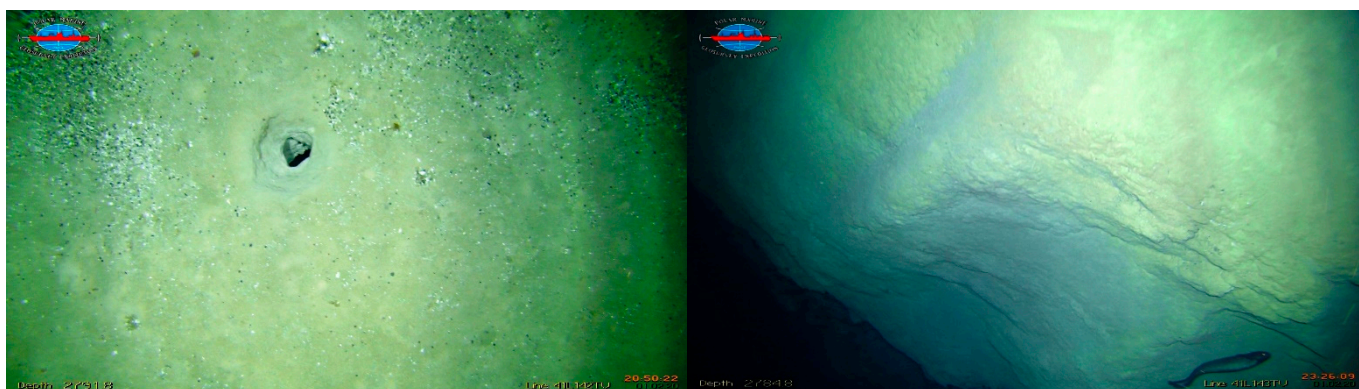


Figure 9. On the (left) the “hole” in the sediments; on the (right) lithified sediments in the upper part of the flank of the fault.

Additionally, an indirect sign of low-temperature hydrothermal activity may be endemic organisms near hydrothermal vents [46], in particular, mollusks *Caliptogena* sp. (Figure 10). Bivalves *Caliptogena* sp. exist in symbiosis with chemoautotrophic thiobacteria and for their existence, numerous elements and compounds (Cu and Zn sulfides, hydrogen, methane, etc.) are needed. Mass accumulation of these organisms may indicate hydrothermal activity, including low-temperature [47].



Figure 10. Massive accumulation of bivalves near the Koralovoye HF.

3.3. CTD-Sounding

CTD-sounding allows us to register the parameters of turbidity, temperature, pressure and electrical conductivity in situ. Deviations of these geophysical fields from the background ocean values indicate active hydrothermal discharge.

Over a long period, we have obtained graphs of the distribution of geophysical parameters near numerous HF's (Figure 11). The vertical distribution of parameters near the bottom at all stations is typical of near-bottom tropical Atlantic water. It is characterized by a close-to-linear trend of a decrease in salinity and temperature and an increase in density with microinversions. Background turbidity values near the bottom, on average, reach values of 0.012–0.024 FTU. Anomalies of a hydrothermal nature distorted the linearity.

Based on the characteristics and signs of geophysical anomalies, we identified six types of complex geophysical anomalies.

The first type is shown in Figure 11a in the ~3020–3080 m, where a neutral buoyancy plume is formed. Negative anomalies of temperature (0.882 °C), salinity (0.0094‰) and density (0.0023 kg/m³), correlating with a turbidity anomaly (0.021 FTU), characterize the plume. The formation of the Atlantic model plume explains the reduced temperature and salinity [38,48]. Mn and Fe form fine colloidal particles [49,50] and spread over considerable distances from the source [51], causing increased turbidity.

Increased turbidity and temperature at a reduced density characterize the second and third types. Salinity anomalies are negative and positive, respectively. This complex anomaly indicates the influence of an ascending hydrothermal plume on the water. The phase differentiation of the hydrothermal fluid under subsurface conditions explains the difference in salinity anomalies. Discharging both the desalinated and mineralized hydrothermal solution was confirmed by sampling the hydrothermal solution near the Logachev HF (29.1–40.2‰). The turbidity anomaly is associated with metal sulfides and hydroxides forming near the source. The reduced density is due to the discharging of a hydrothermal solution saturated with gases of magmatic and metamorphic origins [28,29]. The second type is shown in Figure 11b—a multilayer ascending hydrothermal plume near the Logachev field with positive anomalies of temperature (0.016–0.536 °C) and turbidity (0.027–0.031 FTU), negative anomalies of salinity (0.0025–0.0038‰) and density (0.0032–0.0059 kg/m³). The third type is shown in Figure 11a—a plume near the Ashadze-2 field in the 3140–3170 m with weak positive anomalies of temperature (0.0205 °C and salinity (0.003‰), a decrease in density (0.0014 kg/m³) and a sharp increase in turbidity (0.026 FTU).

The fourth type is an analog of the 3rd, but reflects a fluid with a higher density than the surrounding water, resulting in the formation of a reverse-plume with negative buoyancy [52]. A similar plume was observed earlier near the Logachev field [38].

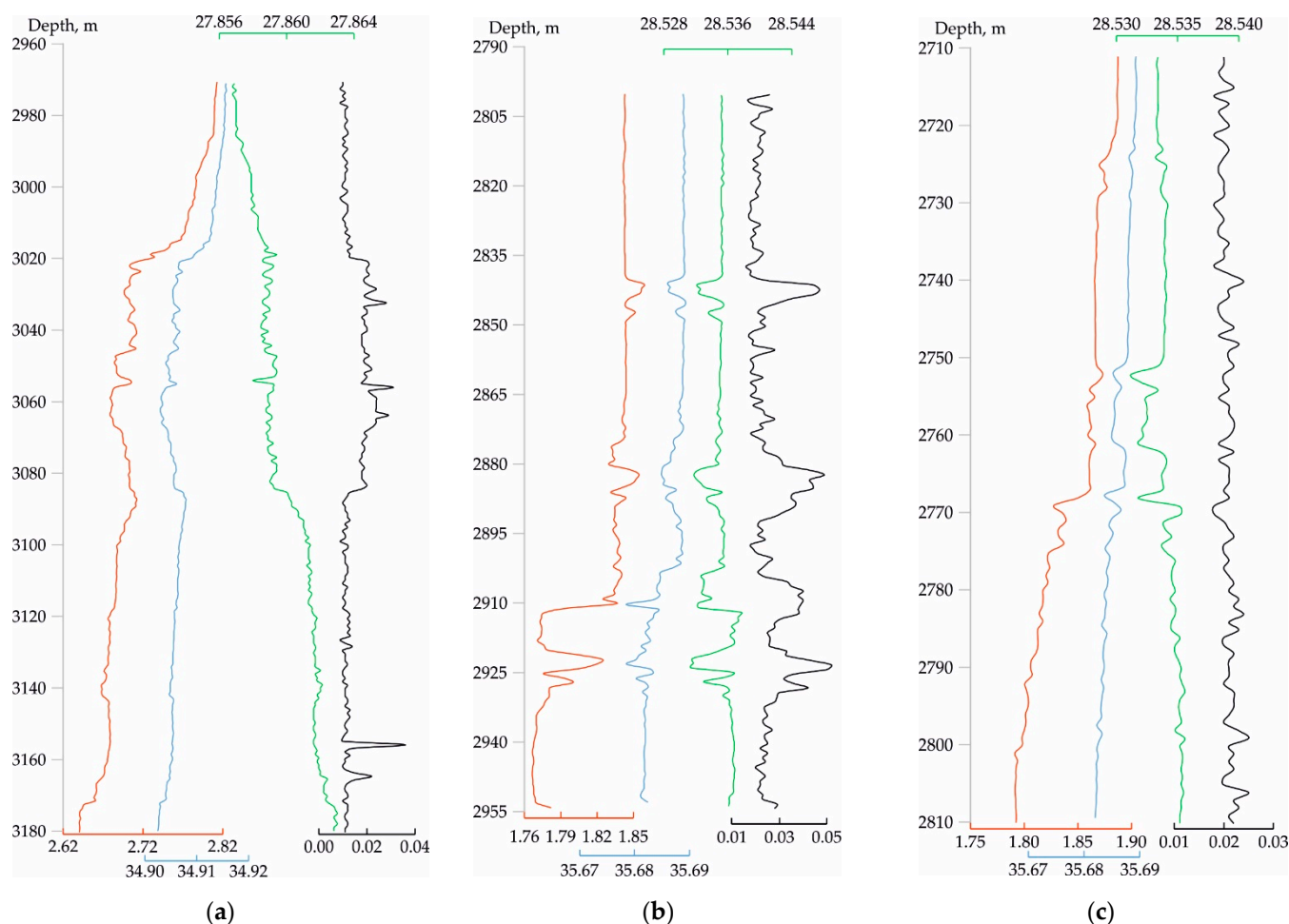


Figure 11. Changes in geophysical parameters near the Logachev (a), Ashadze-2 (b) and Korolovoye (c) HF's: temperature (red, °C), salinity (blue, ‰), density (green, kg/m³), turbidity (black, FTU).

The fifth type is highlighted in Figure 11c, where we note the oscillation of geophysical parameters in 2750–2770 m. Such anomalies are not considered signs of hydrothermal activity and are recognized as insignificant. The oscillation of temperature and salinity disrupts the characteristic linearity of their distribution. The breach with the absence of a turbidity anomaly may indicate low-temperature hydrothermal discharge, which is confirmed by other sensors (e.g., methane sensor) [28].

The sixth type is an anomaly of anthropogenic nature caused, for example, by stirring up sediments. The dredge, cutting into the ground, raises a large amount of sediment that can remain in the water column for a long time. This type was noted near the Peterburgskoye field, where CTD-sounding was performed immediately after the dredging. The average turbidity in the bottom layer was 0.055 FTU, which is a very high value, even for hydrothermal plumes. Simultaneously, the layer of anomalous turbidity directly borders the ocean floor (Figure 12). After 12 days, the sounding station was re-performed at the point where the anomaly was detected. The distribution of all geophysical parameters of the water has changed. First, turbidity returned to the background values. Second, the expressive thermohaline disappeared. Nevertheless, the thermohaline characteristics of the bottom boundary layer (deeper 3000 m) changed slightly. Therefore, at a depth of 3100 m, the following values were recorded at the first station: temperature—2.7105 °C, salinity—34.9188‰, and at the second station: temperature—2.7366 °C, salinity—34.9203‰. CTD sounding makes it possible to detect artificial anomalies of anthropogenic origin and to organize ecological and geochemical monitoring.

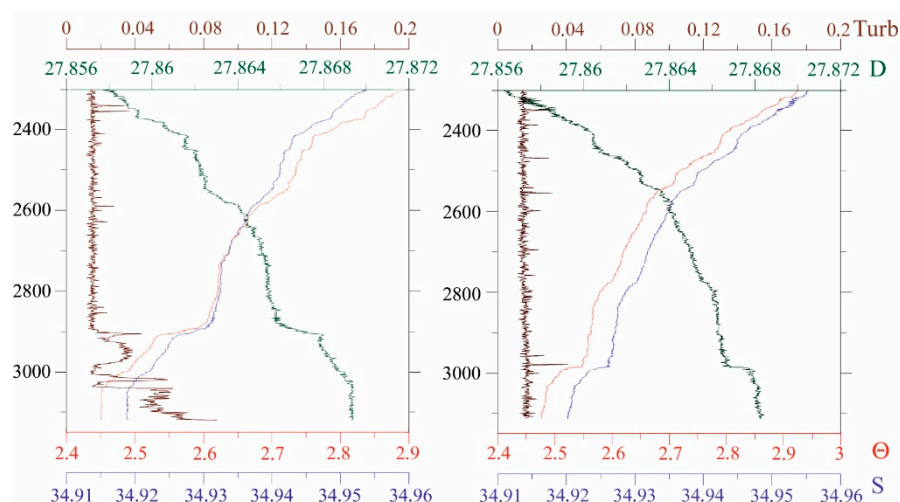


Figure 12. Changes in geophysical parameters near the Peterburgskoye HF: temperature (red, °C), salinity (blue, ‰), density (green, kg/m³), turbidity (brown, FTU). On the (**left**)—sounding immediately after dredging; on the (**right**)—sounding 12 days after dredging.

3.4. Measurements using a Methane Sensor

The methane sensor sounding was performed near the Koralovoye, Molodezhnoye and Logachev HF's together with CTD-sounding.

Methane concentrations near hydrothermal vents were measured numerously in the bottom layer by sampling for subsequent analysis in the laboratory [53–58]. However, this method is limited by the number of samples that can be taken. Measurement of dissolved CH₄ in-situ allows us to accurately record CH₄ concentrations in the water and to understand the structure of the methane anomalies.

3.4.1. Logachev Hydrothermal Cluster

The hydrothermal plume near the Logachev field extends at two levels: 250 and 40 m from the bottom [54]. The sounding station was located close to the Irina-I source (~50 m to the NW). We recorded neutral buoyancy plume and ascending hydrothermal plume [28]. The obtained background concentrations slightly exceeded those obtained in previous studies (2.1–2.5 nM > 1–1.7 nM) [58] and significantly exceeded the background level of the Atlantic Ocean (0.4–0.5 nM) [59]. The maximum methane concentrations (18.7 nM) are less than the CH₄ concentrations found in a plume about 38 m SW of the Smokey Strobe source (113.9 nM) [58].

Zhou et al. noted a methane anomaly (7.14 nM) at ~250–300 m from the bottom at ~440 m to the NW of the Quest source [58]. The anomaly can be the product of the hydrothermal discharge of the Quest source or the result of discharging from an unknown source [58]. Nevertheless, Keir et al. reported a CH₄ anomaly of ~10 nM, more than 10 km north and south of the Logachev HF, at the height of the neutral buoyancy plume spread, while the turbidity anomaly was observed only south of the source [54]. Similar anomalies in amplitude and extent were observed near the Juan de Fuca Ridge and Central Indian Ridge [60,61]. The composition of hydrothermal fluid end-members and source type can explain differences in the concentrations and elevations of methane spreading.

Previous studies have shown that CH₄ anomalies near the Logachev field form well-defined layers at 180–300 m to 500 m from the bottom [54,58]. Our results show methane anomalies at 10–130 m, which is inconsistent with the reported levels of the hydrothermal plume. The separation of the CH₄ anomaly from the bottom, as noted in previous studies, may be related to the stage of cold desalinated waters, which we observed during sounding (Figure 11b). Within this stage (~2910 m and deeper), concentrations rapidly decrease to background values, interrupted by a layer of ascending hydrothermal plume.

3.4.2. Molodezhnoye and Koralovoye HF's

Since the Koralovoye and Molodezhnoye fields were discovered in 2020 [28], methane concentrations have been measured for the first time.

At 200 m to the SE from the Koralovoye field, a weak CH_4 anomaly (up to 5 nM) is associated with a neutral buoyancy plume. At the second station, at ~190 m to the NNE from the source at <50 m from the bottom, a dissolved methane anomaly followed with the absence of geophysical anomalies (Figure 11c). These signs can indicate a possible low-temperature discharge with a high content of CH_4 .

Near the Molodezhnoye field, a weak CH_4 anomaly associates with a plume by analogy to the Koralovoye and Logachev HF's.

Figure 13 shows a comparison of graphs of dissolved CH_4 and turbidity, which is the main sign of hydrothermal activity during sounding [20]. As can be seen from the graphs, CH_4 anomalies have different geometries depending on the type of source and the distance. Methane anomalies do not correlate with geophysical anomalies (turbidity, temperature, salinity). Previously, the absence of a correlation between CH_4 and temperature was noted for the Endeavor hydrothermal site [60]. Surveys within the Central Indian Ridge have shown methane anomalies that are not accompanied by increased turbidity. The authors attribute this to the serpentinization of ultramafic rocks of the oceanic core complexes and not to hydrothermal activity [61].

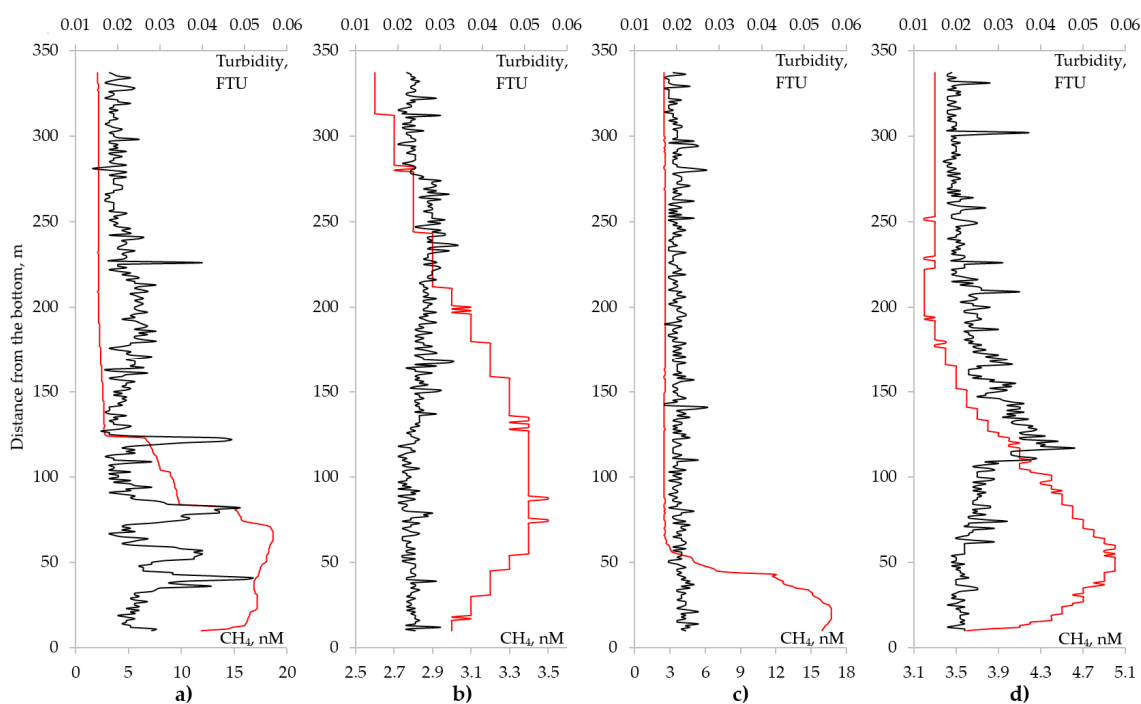


Figure 13. Change in the concentration of dissolved methane (red) and turbidity (black) with depth: (a) 50 m to the NW from the Irina-I vent (Logachev field); (b) 160 m to the NW from the Molodezhnoye field; (c) 190 m to the NNE from the Koralovoye field; (d) 200 m to the SE from the Koralovoye field.

Nevertheless, You O.R. et al. and Kawagucci et al. noted a correlation between CH_4 anomalies within the Central Indian Ridge (Segment 4, 11.3 S and Segment 5, 12.6 S; Dodo HF, 19.5 S and Solitaire HF, 18.4 S) [53,56]. The CH_4 concentrations (~3.3–42.3 nM and ~2–36.7 nM, respectively) are similar to those obtained by us [53,56].

At the moment, the exact location of the hydrothermal vents, the plumes from which were studied in the work of You O.R. et al. [56] is unknown. Due to this, we cannot determine the distance at which the anomalies were detected. Suppose that the maximum concentrations (20 and 42 nM) were obtained close to the source (by analogy with the Logachev field). Then, a decrease in methane concentrations to 3–5 nM occurs at a distance

of 2.3–5.8 km from the intended source, which is less than in other studies [54,60] but still significantly more than in our work.

Based on the coordinates of the sounding stations shown in the work of Kawagucci et al. [53] and the coordinates of the Dodo and Solitaire HF's [62], we determined that elevated concentrations of CH_4 (>5 nM) were detected at a distance of up to 1.5 km from the source, which is the closest to our results.

Based on the results of the sampling of the Logachev hydrothermal fluid end-member [29] and hydrothermal plumes, a schematic structure of methane anomalies was constructed (Figure 14). The maximum concentrations of CH_4 in our work are close to the ocean floor (~50–100 m), below the levels of turbidity anomalies. In the case of low-temperature discharging, methane anomalies are present without any signs of increased turbidity, and the maximum is located at ~20–30 m from the bottom.

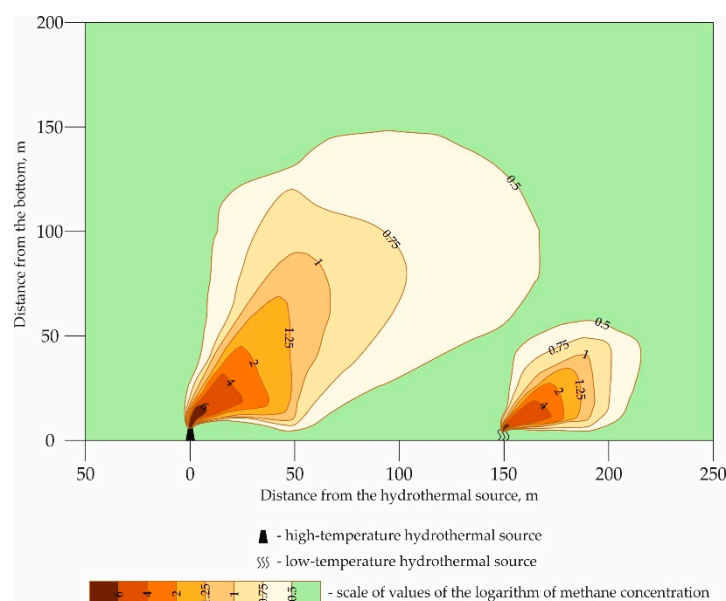


Figure 14. The schematic structure of the methane anomaly over hydrothermal vents based on the results of sounding over the Logachev, Korolovoye and Molodezhnoye fields.

The model constructed by Keir et al. showed that CH_4 concentrations of ~5 nM in the plume are reached at ~4–10 km from the source [54]. This model does not correspond to our results of measuring CH_4 concentrations in situ. The structure of the methane plume shows a small distance and height of the CH_4 distribution, which confirms previous conclusions [58].

Methane released from marine gas hydrates tends to remain in the deep part of the ocean [63,64]. Based on the results of sounding, we conclude that deep-sea hydrothermal CH_4 is also incapable of rising to a great height from the seabed. Methanotrophic archaea and bacteria can actively oxidize CH_4 to CO_2 [65], which can have a significant impact on their distribution near hydrothermal vents.

Dissolved CH_4 can be a reliable marker of modern high- and low-temperature hydrothermal activity. However, the rapid speed of its scattering and variability in the distribution range caused by the influence of numerous factors suggest the need for a dense network of sounding stations or profiles to accurately determine the location of the source.

4. Conclusions

- (1) Profiling by towed vehicles makes it possible to record geophysical (EF) and geochemical anomalies (Eh, pS, etc.). Geophysical anomalies are more often revealed near the bottom, while geochemical anomalies are expressed at 150–200 m from the bottom. Profiling should be conducted in two stages: in the "high" interval to determine

geochemical anomalies and in the “low” interval to identify geophysical anomalies. The EF anomalies in the “low” and “high” intervals have different forms, apparently caused by different reasons—the polarization of the ores and the influence of metal sulfides in the plume, respectively. Geophysical and geochemical anomalies can be separated from each other at distances up to 1000 m, which may be due to the evolution of the plume. EF anomalies are a good search sign of high- and low-temperature discharge and even inactive fields.

- (2) TV profiling allows the detection of direct evidence of high-temperature discharge-hydrothermal structures and smokers’ black “smoke”. Lithification of sediments and accumulation of endemic hydrothermal fauna (e.g., mollusks *Caliptogena* sp.), which can be observed during teleprofiling, may be indirect signs of low-temperature discharge.
- (3) Based on the capacity, amplitude, position and sign of anomalies (turbidity, temperature, salinity and density), we have identified 6 types of complex geophysical anomalies. Types reflect the stage of plume formation, mineralization of end-members of hydrothermal fluid and the cause of its origin (anthropogenic or natural). CTD-sounding is a good method for detecting and verifying hydrothermal anomalies. However, this method cannot detect low-temperature discharging with due accuracy.
- (4) The methane sounding near the Logachev, Korolovoye, Molodezhnoye HF’s and the analysis of published data on CH₄ concentrations in hydrothermal plumes revealed high variability in the behavior of this element. The maximum values of turbidity and methane can be 50–100 m apart from each other, and the height of the rise of CH₄ above the bottom often does not exceed 200–300 m. Elevated concentrations of CH₄ with the absence of distinct geophysical anomalies may indicate low-temperature discharging. The range of CH₄ anomalies depends on several factors and can vary from the first 100 s of meters to the first 10 s of kilometers, thereby complicating the use of a methane sensor in search operations. A dense grid of profiles will allow high- and low-temperature sources to be detected with high accuracy.

Author Contributions: Conceptualization, V.P.; methodology, S.S., V.P., I.D., I.A.; validation, S.S., V.P., E.N., I.D., I.A.; investigation, S.S., V.P., E.N., I.D.; writing—original draft preparation, V.P.; writing—review and editing, V.P. and S.S.; visualization, S.S., V.P., E.N., I.D., I.A. All authors have read and agreed to the published version of the manuscript.

Funding: This research received no external funding.

Data Availability Statement: Data supporting the reported results can be found within the manuscript and is available upon request from the first author.

Acknowledgments: Thanks are owed to the master, crew, and technical staff of the R/V Professor Logachev. We thank the four anonymous reviewers for their constructive feedback, which has improved this contribution.

Conflicts of Interest: The authors declare no conflict of interest.

References

1. Zhang, Z.; Fan, W.; Bao, W.; Chen, C.T.A.; Liu, S.; Cai, Y. Recent developments of exploration and detection of shallow-water hydrothermal systems. *Sustainability* **2020**, *12*, 9109. [[CrossRef](#)]
2. Corliss, J.B.; Dymond, J.; Gordon, L.I.; Edmond, J.M.; von Herzen, R.P.; Ballard, R.D.; Green, K.; Williams, D.; Bainbridge, A.; Crane, K.; et al. Submarine thermal spring on the Galapagos Rift. *Science* **1979**, *203*, 1073–1083. [[CrossRef](#)]
3. Amon, D.J.; Gollner, S.; Morato, T.; Smith, C.R.; Chen, C.; Christiansen, S.; Currie, B.; Drazen, J.C.; Fukushima, T.; Gianni, M.; et al. Assessment of scientific gaps related to the effective environmental management of deep-seabed mining. *Mar. Policy* **2022**, *138*, 105006. [[CrossRef](#)]
4. Hannington, M.; Jamieson, J.; Monecke, T.; Petersen, S.; Beaulieu, S. The abundance of seafloor massive sulfide deposits. *Geology* **2011**, *39*, 1155–1158. [[CrossRef](#)]
5. Singer, D.A. Base and precious metal resources in seafloor massive sulfide deposits. *Ore Geol. Rev.* **2014**, *59*, 66–72. [[CrossRef](#)]
6. Miller, K.A.; Thompson, K.F.; Johnston, P.; Santillo, D. An overview of seabed mining including the current state of development, environmental impacts, and knowledge gaps. *Front. Mar. Sci.* **2018**, *4*, 418. [[CrossRef](#)]

7. Van Dover, C.L.; Arnaud-Haond, S.; Gianni, M.; Helmreich, S.; Huber, J.A.; Jaekel, A.L.; Metaxas, A.; Pendleton, L.H.; Petersen, S.; Ramirez-Llodra, E.; et al. Scientific rationale and international obligations for protection of active hydrothermal vent ecosystems from deep-sea mining. *Mar. Policy* **2018**, *90*, 20–28. [[CrossRef](#)]
8. Douville, E.; Charlou, J.L.; Oelkers, E.H.; Bienvenu, P.; Colon, C.J.; Donval, J.P.; Fouquet, Y.; Prieur, D.; Appriou, P. The rainbow vent fluids (36°14' N, MAR): The influence of ultramafic rocks and phase separation on trace metal content in Mid-Atlantic Ridge hydrothermal fluids. *Chem. Geol.* **2002**, *184*, 37–48. [[CrossRef](#)]
9. Costa, K.M.; Anderson, R.F.; McManus, J.F.; Winckler, G.; Middleton, J.L.; Langmuir, C.H. Trace element (Mn, Zn, Ni, V) and authigenic uranium (aU) geochemistry reveal sedimentary redox history on the Juan de Fuca Ridge, North Pacific Ocean. *Geochim. Cosmochim. Acta* **2018**, *236*, 79–98. [[CrossRef](#)]
10. Mason, J.C.; Branch, A.; Xu, G.; Jakuba, M.V.; German, C.R.; Chien, S.; Bowen, A.D.; Hand, K.P.; Seewald, J.S. Evaluation of AUV Search Strategies for the Localization of Hydrothermal Venting. In Proceedings of the 30th International Conference on Automated Planning and Scheduling (ICAPS 2020), Nancy, France, 26–30 October 2020.
11. Rumynin, V.G.; Nikulenkov, A.M.; Rozov, K.B.; Rozov, K.B.; Erzova, V.A. The status and trends in radioactive contamination of groundwater at a LLW-ILW storage facility site near Sosnovy Bor (Leningrad region, Russia). *J. Environ. Radioact.* **2021**, *237*, 106707. [[CrossRef](#)]
12. Fang, Z.; Wang, W.X. Size speciation of dissolved trace metals in hydrothermal plumes on the Southwest Indian Ridge. *Sci. Total Environ.* **2021**, *771*, 145367. [[CrossRef](#)] [[PubMed](#)]
13. Fouquet, Y.; Cambon, P.; Etoubleau, J.; Charlou, J.L.; Ondréas, H.; Barriga, F.J.; Cherkashov, G.; Semkova, T.; Poroshina, I.; Bohn, M. Geodiversity of Hydrothermal Processes along the Mid-Atlantic Ridge and Ultramafic-Hosted Mineralization: A New Type of Oceanic Cu-Zn-Co-Au Volcanogenic Massive Sulfide Deposit. In *Diversity of Hydrothermal Systems on Slow Spreading Ocean Ridges*; American Geophysical Union: Washington, DC, USA, 2013; Volume 188, pp. 321–367.
14. Liao, S.; Tao, C.; Dias, Á.A.; Su, X.; Yang, Z.; Ni, J.; Liang, J.; Yang, W.; Liu, J.; Li, W.; et al. Surface sediment composition and distribution of hydrothermal derived elements at the Duanqiao-1 hydrothermal field, Southwest Indian Ridge. *Mar. Geol.* **2019**, *416*, 105975. [[CrossRef](#)]
15. Lough, A.J.M.; Homoky, W.B.; Connelly, D.P.; Comer-Warner, S.A.; Nakamura, K.; Abyaneh, M.K.; Kaulich, B.; Mills, R.A. Soluble iron conservation and colloidal iron dynamics in a hydrothermal plume. *Chem. Geol.* **2019**, *511*, 225–237. [[CrossRef](#)]
16. Reeves, E.P.; McDermott, J.M.; Seewald, J.S. The origin of methanethiol in midocean ridge hydrothermal fluids. *Proc. Natl. Acad. Sci. USA* **2014**, *111*, 5474–5479. [[CrossRef](#)] [[PubMed](#)]
17. Voitekhovskiy, Y.L.; Zakharova, A.A. Petrographic structures and Hardy-Weinberg equilibrium. *J. Min. Inst.* **2020**, *242*, 133–138. [[CrossRef](#)]
18. Wankel, S.D.; Germanovich, L.N.; Lilley, M.D.; Genc, G.; DiPerna, C.J.; Bradley, A.S.; Olson, E.J.; Girguis, P.R. Influence of subsurface biosphere on geochemical fluxes from diffuse hydrothermal fluids. *Nat. Geosci.* **2011**, *4*, 461–468. [[CrossRef](#)]
19. Perner, M.; Gonnella, G.; Hourdez, S.; Böhnke, S.; Kurtz, S.; Girguis, P. In situ chemistry and microbial community compositions in five deep-sea hydrothermal fluid samples from Irina II in the Logatchev field. *Environ. Microbiol.* **2013**, *15*, 1551–1560. [[CrossRef](#)]
20. Tao, C.; Chen, S.; Baker, E.T.; Li, H.; Liang, J.; Liao, S.; Chen, Y.J.; Deng, X.; Zhang, G.; Gu, C.; et al. Hydrothermal plume mapping as a prospecting tool for seafloor sulfide deposits: A case study at the Zouyu-1 and Zouyu-2 hydrothermal fields in the southern Mid-Atlantic Ridge. *Mar. Geophys. Res.* **2017**, *38*, 3–16. [[CrossRef](#)]
21. Escartin, J.; Mevel, C.; Petersen, S.; Bonnemains, D.; Cannat, M.; Andreani, M.; Augustin, A.; Bezos, A.; Chavagnac, V.; Choi, Y.; et al. Tectonic structure, evolution, and the nature of oceanic core complexes and their detachment fault zones (13°20' N and 13°30' N, Mid Atlantic Ridge). *Geochem. Geophys. Geosystems* **2017**, *18*, 1451–1482. [[CrossRef](#)]
22. MacLeod, C.J.; Searle, R.C.; Murton, B.J.; Casey, J.F.; Mallow, C.; Unsworth, S.C.; Achenbach, K.L.; Harris, M. Life cycle of oceanic core complexes. *Earth Planet. Sci. Lett.* **2009**, *287*, 333–344. [[CrossRef](#)]
23. Bel'tenev, V.; Shagin, A.; Markov, V.; Rozhdestvenskaya, I.; Stepanova, T.; Cherkashev, G.; Fedorov, I.; Rummyantsev, A.; Poroshina, I. A new hydrothermal field at 16°38.4' N, 46°28.5' W on the Mid-Atlantic Ridge. *InterRidge News* **2004**, *13*, 5–6.
24. Cherkashov, G.; Bel'tenev, V.; Ivanov, V.; Lazareva, L.; Samovarov, M.; Shilov, V.; Stepanova, T.; Glasby, G.P.; Kuznetsov, V. Two new hydrothermal fields at the Mid-Atlantic Ridge. *Mar. Georesources Geotechnol.* **2008**, *26*, 308–316. [[CrossRef](#)]
25. Shilov, V.V.; Bel'tenev, V.E.; Ivanov, V.N.; Cherkashev, G.A.; Rozhdestvenskaya, I.I.; Gablina, I.F.; Dobretsova, I.G.; Narkevskii, E.V.; Gustaitis, A.N.; Kuznetsov, V.Y. New hydrothermal ore fields in the Mid-Atlantic Ridge: Zenith-Victoria (20°08' N) and Petersburg (19°52' N). *Dokl. Earth Sci.* **2012**, *442*, 63. [[CrossRef](#)]
26. Cherkashov, G.; Poroshina, I.; Stepanova, T.; Ivanov, V.; Bel'tenev, V.; Lazareva, L.; Rozhdestvenskaya, I.; Samovarov, M.; Shilov, V.; Glasby, G.P.; et al. Seafloor massive sulfides from the northern equatorial Mid-Atlantic Ridge: New discoveries and perspectives. *Mar. Georesources Geotechnol.* **2010**, *28*, 222–239. [[CrossRef](#)]
27. Bel'tenev, V.E.; Lazareva, L.I.; Cherkashev, G.A.; Ivanov, V.I.; Rozhdestvenskaya, I.I.; Kuznetsov, V.A.; Laiba, A.A.; Narkevskiy, E.V. New hydrothermal sulfide fields of the Mid-Atlantic Ridge: Yubileinoe (20°09' N) and Surprise (20°45.4' N). *Dokl. Earth Sci.* **2017**, *476*, 1010–1015. [[CrossRef](#)]
28. Sudarikov, S.; Narkevskiy, E.; Petrov, V. Identification of Two New Hydrothermal Fields and Sulfide Deposits on the Mid-Atlantic Ridge as a Result of the Combined Use of Exploration Methods: Methane Detection, Water Column Chemistry, Ore Sample Analysis, and Camera Surveys. *Minerals* **2021**, *11*, 726. [[CrossRef](#)]

29. Fouquet, Y.; Cherkashov, G.; Charlou, J.L.; Ondréas, H.; Birot, D.; Cannat, M.; Bortnikov, N.; Silantyev, S.; Sudarikov, S.; Cambon-Bonavita, M.A.; et al. Serpentine Cruise—Ultramafic hosted hydrothermal deposits on the Mid-Atlantic Ridge: First submersible studies on Ashadze 1 and 2, Logatchev 2 and Krasnov vent fields. *InterRidge News* **2008**, *17*, 15–20.
30. Ondréas, H.; Cannat, M.; Fouquet, Y.; Normand, A. Geological context and vents morphology of the ultramafic-hosted Ashadze hydrothermal areas (Mid-Atlantic Ridge 13° N). *Geochem. Geophys. Geosystems* **2012**, *13*, 20. [[CrossRef](#)]
31. Krasnov, S.G.; Cherkashev, G.A.; Stepanova, T.V.; Batuyev, B.N.; Krotov, A.G.; Malin, B.V.; Maslov, M.N.; Markov, V.F.; Poroshina, I.M.; Samovarov, M.S.; et al. Detailed geological studies of hydrothermal fields in the North Atlantic. *Geol. Soc. Lond. Spec. Publ.* **1995**, *87*, 43–64. [[CrossRef](#)]
32. Kuhn, T.; Ratmeyer, V.; Petersen, S.; Hekinian, R.; Koschinsky, A.; Seifert, R.; Borowski, C.; Imhoff, J.F.; Türkay, M.; Herzig, P.; et al. The Logatchev hydrothermal field-revisited: New findings of the R/V Meteor cruise HYDROMAR I (M60/3). *InterRidge News* **2004**, *13*, 1–4.
33. Cherkashov, G.; Kuznetsov, V.; Kuksa, K.; Tabuns, E.; Maksimov, F.; Bel'tenev, V. Sulfide geochronology along the northern equatorial Mid-Atlantic Ridge. *Ore Geol. Rev.* **2017**, *87*, 147–154. [[CrossRef](#)]
34. Gablina, I.F.; Dobretzova, I.G.; Laiba, A.A.; Narkevsky, E.V.; Maksimov, F.E.; Kuznetsov, V.Y. Specific features of sulfide ores in the Pobeda hydrothermal cluster, Mid-Atlantic Rise 17°07'–17°08' N. *Lithol. Miner. Resour.* **2018**, *53*, 431–454. [[CrossRef](#)]
35. Beltenev, V.; Ivanov, V.; Rozhdestvenskaya, I.; Cherkashov, G.; Stepanova, T.; Shilov, V.; Pertsev, A.; Davydov, M.; Egorov, I.; Melekestseva, I.; et al. A new hydrothermal field at 13 30' N on the Mid-Atlantic Ridge. *InterRidge News* **2007**, *16*, 9–10.
36. Beaulieu, S.E.; Baker, E.T.; German, C.R. Where are the undiscovered hydrothermal vents on oceanic spreading ridges? *Deep Sea Res. Part II Top. Stud. Oceanogr.* **2015**, *121*, 202–212. [[CrossRef](#)]
37. Baker, E.T.; Resign, J.A.; Haymon, R.M.; Tunncliffe, V.; Lavelle, J.W.; Martinez, F.; Ferrini, V.; Walker, S.L.; Nakamura, K. How many vent fields? New estimates of vent field populations on ocean ridges from precise mapping of hydrothermal discharge locations. *Earth Planet. Sci. Lett.* **2016**, *449*, 186–196. [[CrossRef](#)]
38. Sudarikov, S.M.; Roumiantsev, A.B. Structure of hydrothermal plumes at the Logatchev vent field, 14°45' N, Mid-Atlantic Ridge: Evidence from geochemical and geophysical data. *J. Volcanol. Geotherm. Res.* **2000**, *101*, 245–252. [[CrossRef](#)]
39. Gablina, I.F.; Popova, E.A.; Sadchikova, T.A.; Savichev, A.T.; Gor'kova, N.V.; Os'kina, N.S.; Khusid, T.A. Hydrothermal metasomatic alteration of carbonate bottom sediments in the Ashadze-1 field (13° N Mid-Atlantic Ridge). *Geol. Ore Depos.* **2014**, *56*, 357–379. [[CrossRef](#)]
40. Batuyev, B.N.; Krotov, A.G.; Markov, V.F.; Cherkashev, G.A.; Krasnov, S.G.; Lisitsyn, Y.D. Massive sulphide deposits discovered and sampled at 14°45' N, Mid-Atlantic Ridge. *BRIDGE Newsl.* **1994**, *6*, 6–10.
41. German, C.R.; Thurnherr, A.M.; Knoery, J.; Charlou, J.L.; Jean-Baptiste, P.; Edmonds, H.N. Heat, volume and chemical fluxes from submarine venting: A synthesis of results from the Rainbow hydrothermal field, 36 N MAR. *Deep Sea Res. Part I Oceanogr. Res. Pap.* **2010**, *57*, 518–527. [[CrossRef](#)]
42. Field, M.P.; Sherrell, R.M. Dissolved and particulate Fe in a hydrothermal plume at 9 45' N, East Pacific Rise: Slow Fe (II) oxidation kinetics in Pacific plumes. *Geochim. Cosmochim. Acta* **2000**, *64*, 619–628. [[CrossRef](#)]
43. Rudnicki, M.D.; Elderfield, H. A chemical model of the buoyant and neutrally buoyant plume above the TAG vent field, 26 degrees N, Mid-Atlantic Ridge. *Geochim. Cosmochim. Acta* **1993**, *57*, 2939–2957. [[CrossRef](#)]
44. Schmittner, A.; Galbraith, E.D.; Hostetler, S.W.; Pedersen, T.F.; Zhang, R. Large fluctuations of dissolved oxygen in the Indian and Pacific oceans during Dansgaard-Oeschger oscillations caused by variations of North Atlantic Deep Water subduction. *Paleoceanography* **2007**, *22*, PA3207. [[CrossRef](#)]
45. Gerdes, K.; Martínez Arbizu, P.; Schwarz-Schampera, U.; Schwentner, M.; Kihara, T.C. Detailed mapping of hydrothermal vent fauna: A 3D reconstruction approach based on video imagery. *Front. Mar. Sci.* **2019**, *6*, 96. [[CrossRef](#)]
46. Sudarikov, S.M.; Yungmeister, D.A.; Korolev, R.I.; Petrov, V.A. On the possibility of reducing man-made burden on benthic biotic communities when mining solid minerals using technical means of various designs. *J. Min. Inst.* **2022**, *253*, 82–96. [[CrossRef](#)]
47. Demina, L.L.; Galkin, S.V.; Krylova, E.M.; Budko, D.F.; Solomatina, A.S. Some Biogeochemical Characteristics of the Trace Element Bioaccumulation in the Benthic Fauna of the Piip Volcano (The Southwestern Bering Sea). *Minerals* **2021**, *11*, 1233. [[CrossRef](#)]
48. Speer, K.G.; Rona, P.A. A model of an Atlantic and Pacific hydrothermal plume. *J. Geophys. Res. Ocean.* **1989**, *94*, 6213–6220. [[CrossRef](#)]
49. Saager, P.M.; De Baar, H.J.; de Jong, J.T.; Nolting, R.F.; Schijf, J. Hydrography and local sources of dissolved trace metals Mn, Ni, Cu, and Cd in the northeast Atlantic Ocean. *Mar. Chem.* **1997**, *57*, 195–216. [[CrossRef](#)]
50. Sander, S.G.; Koschinsky, A. Metal flux from hydrothermal vents increased by organic complexation. *Nat. Geosci.* **2011**, *4*, 145–150. [[CrossRef](#)]
51. Resing, J.A.; Sedwick, P.N.; German, C.R.; Jenkins, W.J.; Moffett, J.W.; Sohst, B.M.; Tagliabue, A. Basin-scale transport of hydrothermal dissolved metals across the South Pacific Ocean. *Nature* **2015**, *523*, 200–203. [[CrossRef](#)]
52. Woods, A.W. Turbulent plumes in nature. *Annu. Rev. Fluid Mech.* **2010**, *42*, 391–412. [[CrossRef](#)]
53. Kawagucci, S.; Okamura, K.; Kiyota, K.; Tsunogai, U.; Sano, Y.; Tamaki, K.; Gamo, T. Methane, manganese, and helium-3 in newly discovered hydrothermal plumes over the Central Indian Ridge, 18°–20° S. *Geochem. Geophys. Geosystems* **2008**, *9*, Q10002. [[CrossRef](#)]
54. Keir, R.S.; Schmale, O.; Seifert, R.; Sültenfuß, J. Isotope fractionation and mixing in methane plumes from the Logatchev hydrothermal field. *Geochem. Geophys. Geosystems* **2009**, *10*, Q05005. [[CrossRef](#)]

55. Wen, H.Y.; Sano, Y.; Takahata, N.; Tomonaga, Y.; Ishida, A.; Tanaka, K.; Kagoshima, T.; Shirai, K.; Ishibashi, J.-I.; Yokose, H.; et al. Helium and methane sources and fluxes of shallow submarine hydrothermal plumes near the Tokara Islands, Southern Japan. *Sci. Rep.* **2016**, *6*, 34126. [[CrossRef](#)]
56. You, O.R.; Son, S.K.; Baker, E.T.; Son, J.; Kim, M.J.; Barcelona, M.J.; Kim, M. Bathymetric influence on dissolved methane in hydrothermal plumes revealed by concentration and stable carbon isotope measurements at newly discovered venting sites on the Central Indian Ridge (11–13 S). *Deep Sea Res. Part I Oceanogr. Res. Pap.* **2014**, *91*, 17–26. [[CrossRef](#)]
57. Zhang, X.; Sun, Z.; Wang, L.; Zhang, X.; Zhai, B.; Xu, C.; Geng, W.; Cao, H.; Yin, X.; Wu, N. Distribution and discharge of dissolved methane in the middle Okinawa Trough, East China Sea. *Front. Earth Sci.* **2020**, *8*, 333. [[CrossRef](#)]
58. Zhou, H.; Wu, Z.; Peng, X.; Jiang, L.; Tang, S. Detection of methane plumes in the water column of Logatchev hydrothermal vent field, Mid-Atlantic Ridge. *Chin. Sci. Bull.* **2007**, *52*, 2140–2146. [[CrossRef](#)]
59. Charlou, J.L.; Donval, J.P. Hydrothermal methane venting between 12° N and 26° N along the Mid-Atlantic Ridge. *J. Geophys. Res. Solid Earth* **1993**, *98*, 9625–9642. [[CrossRef](#)]
60. Cowen, J.P.; Wen, X.; Popp, B.N. Methane in aging hydrothermal plumes. *Geochim. Cosmochim. Acta* **2002**, *66*, 3563–3571. [[CrossRef](#)]
61. Son, J.; Pak, S.J.; Kim, J.; Baker, E.T.; You, O.R.; Son, S.K.; Moon, J.W. Tectonic and magmatic control of hydrothermal activity along the slow-spreading Central Indian Ridge, 8° S–17° S. *Gechem. Geophys. Geosystems* **2014**, *15*, 2011–2020. [[CrossRef](#)]
62. Nakamura, K.; Watanabe, H.; Miyazaki, J.; Takai, K.; Kawagucci, S.; Noguchi, T.; Nemoto, S.; Watsuji, T.; Matsuzaki, T.; Shibuya, T.; et al. Discovery of new hydrothermal activity and chemosynthetic fauna on the Central Indian Ridge at 18–20 S. *PLoS ONE* **2012**, *7*, e32965. [[CrossRef](#)]
63. Elliott, S.; Maltrud, M.; Reagan, M.; Mordis, G.; Cameron-Smith, P. Marine methane cycle simulations for the period of early global warming. *J. Geophys. Res. Biogeosciences* **2011**, *116*, G01010.
64. Ruppel, C.D.; Kessler, J.D. The interaction of climate change and methane hydrates. *Rev. Geophys.* **2017**, *55*, 126–168. [[CrossRef](#)]
65. Leonte, M.; Kessler, J.D.; Kellermann, M.Y.; Arrington, E.C.; Valentine, D.L.; Sylva, S.P. Rapid rates of aerobic methane oxidation at the feather edge of gas hydrate stability in the waters of Hudson Canyon, US Atlantic Margin. *Geochim. Cosmochim. Acta* **2017**, *204*, 375–387. [[CrossRef](#)]